MICHIGAN STATE UNIVERSITY

CYCLOTRON LABORATORY

# THE EFFECT OF SPACE CHARGE FORCE ON BEAMS EXTRACTED FROM ECR ION SOURCES

ZU QI XIE

Ph.D. Dissertation

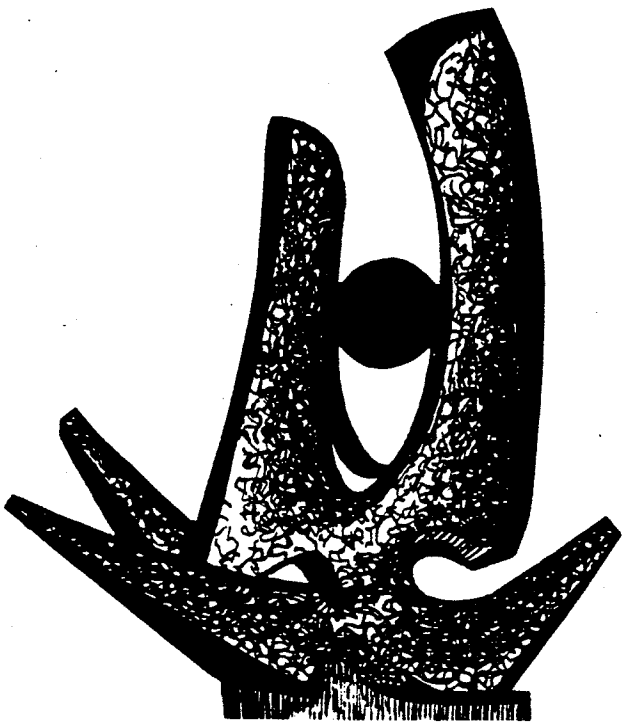

OCTOBER 1989

MSUCP-60

MSUCP-60
October, 1989

# THE EFFECT OF SPACE CHARGE FORCE ON BEAMS EXTRACTED FROM ECR ION SOURCES

by

Zu Qi Xie

Ph.D. Dissertation

Michigan State University

1989

# THE EFFECT OF SPACE CHARGE FORCE ON BEAMS EXTRACTED FROM ECR ION SOURCES

by

Zu Qi Xie

A DISSERTATION

Submitted to
Michigan State University
in partial fulfillment of the requirements
for the degree of

DOCTOR OF PHILOSOPHY

Department of Physics and Astronomy

1989

LIST OF FIGURES

# Chapter 1

# Introduction

## 1.1 Motivation

The ECRIS (Electron Cyclotron Resonance Ion Source, an introduction to the ECRIS is presented in the Appendix), is now the most frequently used new ion source for producing high charge state positive ions for accelerators and for atomic physics research. ECRIS originated from plasma fusion developments in the late 1960's and early 1970's. Observations were made as early as 1969 in during the use of ECRH (Electron Cyclotron Resonance Heating) in plasma devices to produce high charge state ions [Ge70,Po70], and the early extracted beams from these devices were reported in 1972 [Bl72,Wo72]. Following the pioneering work of R. Geller and his coworkers at Centre D'etudes Nucleaires de Grenoble, France, where the ECRIS originated, there are now about 40 ECRIS in operation or under construction around the world. The coupling of ECRIS to cyclotrons has resulted in significant performance gains in energy, intensity, reliability and in the variety of ion species available. At least five ECRIS have been dedicated for atomic physics research, and at many facilities atomic physics programs share ECRIS with nuclear science programs. Although ECRIS have wide application, it is still a relatively young technology. The dynamical processes are still not understood in detail. Important unknowns include the detailed mechanism of microwave coupling for electron heating, the nature of ion heating in the plasma and the effect on ion confinement, the systematics of the



gas mixing effect [Dr85, Ma86a, An88], and the relationships between the emittance of the beams extracted from the ECRIS and the magnetic field, charge state, ion mass, ion thermal energy, space charge force and electron neutralization and so on. Further development of ECRIS will require greater understanding of these and other important issues. For ECRIS coupled to accelerators, the last area mentioned above, the beam formation process, is critical to the design and operation of the accelerator coupling line.

Most ECRIS have been built for multiply-charged positive ion injection into accelerators. The sources and injection lines generally must operate over a broad range of charges and intensities; the injection rigidity is generally set by accelerator characteristics. The pressure in the coupling line between ECRIS and accelerator is low because the ECRIS main stage pressure is low, in the range of $10^{-7}$ T, and it is desirable to avoid the beamline constitute a source of gas for the main stage operation. The specifications for the beam transport elements are generally obtained by assuming (or extrapolating from existing data) a starting emittance at the source extraction aperture, and tracking that emittance with transport optics codes up to a match condition near the accelerator.

Generally beams are extracted DC from ECRIS. If the charge within an ion beam is not neutralized, then the charge density in space is not zero. The consequence of this nonzero charge density is that it creates an electric field within the extracted beam. For a DC ion beam with rotational symmetry, this force is predominantly outward and it will cause the beam to expand in diameter and continuously change the beam divergence due to the repulsion effects. Such space

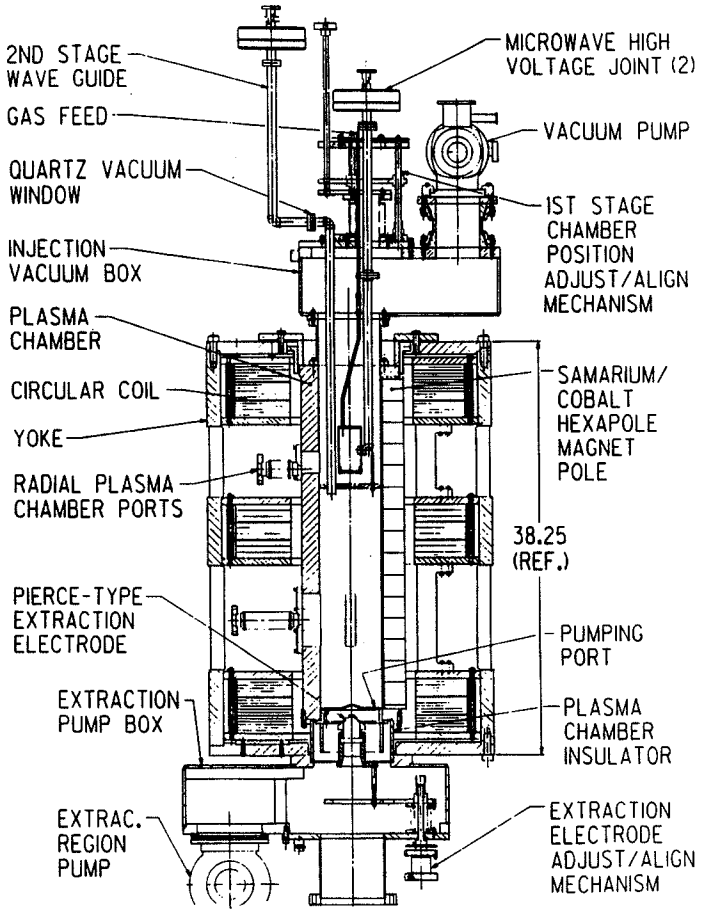


Figure 1.1. A schematic diagram showing the main features of the RTECR ion source.



**Table 1.1**

**RTECR source DC performance for gaseous feed materials**

| q | $^{12}C$ | $^{14}N$ | $^{16}O$ | $^{20}Ne$ | $^{40}Ar$ | $^{86}Kr$ | $^{129}Xe$ | $^{127}I$ |
|---|---|---|---|---|---|---|---|---|
| 4 | 25.5 | 100. | 87. | 67. | 19. | | | |
| 5 | 5.6 | 68. | 61. | 50.5 | * | | | |
| 6 | * | 25.5 | 52. | 41.1 | 42. | | | |
| 7 | | * | 12.2 | 16.5 | 55. | | | |
| 8 | | | * | 5.0 | 94. | | | |
| 9 | | | | 1.0 | 44. | | | |
| 10 | | | | * | * | 23. | | |
| 11 | | | | | 7.6 | * | | |
| 12 | | | | | 2.0 | 23.3 | 2.3 | |
| 13 | | | | | .33 | 29.0 | 2.5 | 1.7 |
| 14 | | | | | .15 | 29.0 | 2.7 | 2.3 |
| 15 | | | | | | 23.2 | 2.9 | 3.0 |
| 16 | | | | | | * | 3.1 | * |
| 17 | | | | | | 6.8 | 3.0 | 2.7 |
| 18 | | | | | | 3.2 | 2.7 | * |
| 19 | | | | | | 1.4 | 2.3 | 2.5 |
| 20 | | | | | | 0.4 | 1.4 | 2.3 |
| 21 | | | | | | | 0.8 | 2.1 |
| 22 | | | | | | | .45 | 1.8 |
| 23 | | | | | | | .20 | 1.0 |
| 24 | | | | | | | .11 | * |
| 25 | | | | | | | | .035 |

Conditions: 10 kV extraction voltage; 8 mm extraction aperture;
All currents in unit eμA.

* Mixed Q/M.

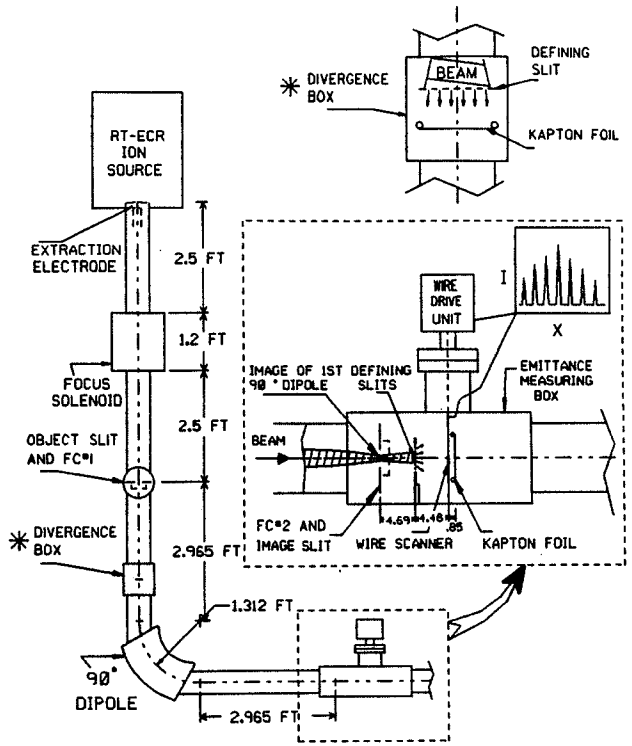


Figure 1.2. A schematic view of the RTECR analysis system and the beam analysis systems built for the studies presented in this thesis.



first acceleration gap optimized at the maximum possible value of 3.3 cm with zero voltage on the decel electrode. The hard edge emittance [De83, Ha87] of a helium 1+ beam after extraction should be expected to be 70 - 100 mm mrad at 10 kV for an 8 mm extraction aperture and B = 2.5 kG, but all early measurements of the emittance after the solenoid were much higher [An88]. With an analysis acceptance of about 300 mm mrad, the dipole image was always about twice the object size, suggesting aberrations, and the overall transmission, measured as the ratio of FC#2 peak currents to the net extracted current (source bias current minus the drain current for no plasma or puller current), or as $\sum$FC#2/$\sum$FC#1, was about 40 - 45%. The cause of this overall low transmission, typical for many ECR sources [An89], was not understood.

### 1.3 He Beam Technique

We have found that helium plasmas, tuned to maximize the helium 1+, provide good beams for studying the beam formation process in the RTECR. There is a large enough difference in source conditions for helium 2+, such that the total extracted current is at least 90-95% helium 1+, as shown in the spectrum in Figure 1.3. In this regard hydrogen does not work as well - $H_2^+$ and $H^+$ production are more closely coupled in ECRIS, and of course any heavier mass species will have a distribution of extracted charges. The RTECR has a wide dynamic range of helium 1+ production - from a few microamps to milliamps, even at fixed low microwave power and essentially constant magnetic field. The required microwave power is $\leq$ 100 watts, while we typically use 1.2 kW for high charge argon ion production. We expect low thermal

# Chapter 2

# The BEAM_3D Code

## 2.1 Motivation

As mentioned previously, ECRIS for multiply-charged ions can produce multiple ion species simultaneously. The beam formation process involves the electric fields produced by the extraction electrodes, magnetic fields from source solenoid coils, iron yoke and multipole magnets, the charge state distribution (CSD), space charge force, the plasma boundary, the ion thermal energy and beam neutralization. One would like to know what parameters are the most important for beam quality and accelerator transport matching. To answer this question, one generally makes simplifying assumptions. The typical assumptions made are to study only a single ion species and azimuthal field symmetry, in order to reduce the calculations or apply an existing code, such as the SLAC Electron Trajectory Code [He79]. One exception would be KOBRA3, developed at GSI, in which some calculations were done in 3D for ECRIS extraction [Sp85], but only with extraction of the single species $O^{3+}$. However, the existing codes do not include the total magnetic field in an ECRIS extraction region in a 3D calculation of the ion trajectories, while also taking the other parameters mentioned above into consideration at the same time. In order to support theoretically the ECRIS beam extraction experimental measurements of this dissertation, a new code, BEAM_3D has been developed.



## 2.2 General Organization

Shown in Figure 2.1 is a flow chart of the present BEAM_3D code. First, primary data input, such as the field data files (which will be explained in later section), CSD, ion thermal energy, extraction voltages and the focussing solenoid specifications. Second, ion ray tracing in the combined fields is performed with an axial step size of a few tenths mm to 1 mm, and a sequential output data file is generated. Third, a routine evaluates the emittances at requested locations and prepares a plot data output file. Fourth, graphic output, including ion trajectories in actual dimensions, is generated on a line printer.

Details involved in these calculations are presented below.

1. Assumptions

The present operating code is based on the following assumptions: (1) the space charge force has only a radial component; (2) the volume charge density in the region of a very short cylinder beam of radius r is constant.

2. Starting conditions

The code can handle up to 300 rays (or more if the computer memory space is available) with different Q/M ion species, each ray is partitioned, by input, with a portion of the total starting current. The plasma boundary is not taken into consideration yet due to lack of detailed knowledge. The ions are emitted from a plane at the chamber side of the extraction aperture perpendicular to the optical axis. The initial particle positions can be input or uniformly generated by

4. Interpolation of the External Fields

The electric fields of the extraction electrodes and magnetic fields due to the solenoid coils and iron yoke, which have azimuthal symmetry, are calculated by the POISSON code [Ho79] with a small mesh spacing in the r and z directions. The fields at a point P(r,z) between grid points, as shown in Figure 2.2, are linearly interpolated using the following two dimensional formulae [Xi87]

$$Fz(r,z) = \frac{(r-r_1)}{(r_2-r_1)(z_3-z_1)}\,[(Fz_4+Fz_1-Fz_3-Fz_2)(z-z_1)+(Fz_2-Fz_1)(z_3-z_1)] + \frac{(Fz_3-Fz_1)}{(z_3-z_1)}\,(z-z_1)+Fz_1 \qquad (2.4)$$

$$Fr(r,z) = \frac{(z-z_1)}{(r_2-r_1)(z_3-z_1)}\,[(Fr_4+Fr_1-Fr_3-Fr_2)(r-r_1)+(Fr_3-Fr_1)(r_2-r_1)] + \frac{(Fr_2-Fr_1)}{(r_2-r_1)}\,(r-r_1)+Fr_1 \qquad (2.5)$$

where $\vec{F}$ stands for $\vec{E}$ or $\vec{B}$ field.

By using POISSON for the magnetic field generation, BEAM_3D automatically takes into consideration any iron included in the problem. The hexapole field is incorporated into the total magnetic field by calling a subroutine "HEX" [Xi86]. Our BEAM_3D calculations have shown, however that the effect of the hexapole field on the beam formation is on the order of 1%, because the hexapole strength up to the typical extraction aperture radius is much less than the solenoid coil strength. So BEAM_3D calculations are usually done without the hexapole field to speed up the calculation.



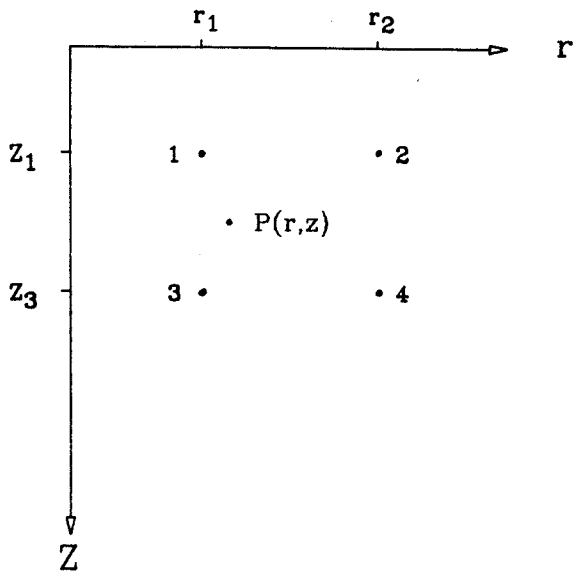


Figure 2.2. This figure shows the grid points involved in the interpolation of field components of an intermediate point P(r,z).

estimate the space charge force on each ray, BEAM_3D recomputes the space charge force on each ray by counting only the current enclosed by its orbit.

6. Geometry of Calculation

BEAM_3D will track the beam from the source extraction region through the first focussing solenoid and a beam collimating slit down to the entrance of the 1st 90° analysis magnet as shown in Figure 2.4. The z-axis is taken as the beamline optical axis. In the initial beamline, after the source extraction electrodes, is an X-Y steering magnet (which is not taken into consideration in this code, and was generally set to zero for beam studies), followed by the focussing solenoid. A beam defining slit is located at the image of the focussing solenoid and this image is the object of the 1st 90° analysis magnet. Computing the beam trajectories through the focussing solenoid to the entrance of the 90° magnet is very essential, as will be seen, for a proper matching of the ion source extraction to the beam transport system.

7. Output Form

Figures 2.5 - 2.8 show the graphic outputs of a helium beam calculation. The orbits of the ions are plotted in the r-z plane, with the extraction electrodes, shown in Figure 2.5, the focussing solenoid and the beam defining slit indicated at the proper locations as well as the ion orbits in the transverse X-Y plane. In this calculation of both $He^{1+}$ and $He^{2+}$ ions, $He^{2+}$ is over-focused because the solenoid is set for $He^{1+}$ transport and hits the beam pipe and the



beam defining slit. The initial and final ion position distributions are shown in Figure 2.6, while Figure 2.7 shows the initial and final CSD and the emittance fittings are shown in Figure 2.8.

## 2.3 Special Features

The special features of the BEAM_3D code are summarized as follows:

1. The CSD can be artificially specified or based on source measurements. The focussing solenoid current is set for the focussing requirements of a selected ion species. In order to have a better simulation of the beam extraction and transport, the space charge force is determined by the distribution of multiple ion species. For a specific solenoid focussing power, some ion species will be over-focused, possibly hitting the beam pipe at some locations, while other species will be under-focused, which, depending upon exact conditions, will go through or hit the beam defining slit. Ions that are stopped by these mechanical structures are removed from consideration, the CSD is adjusted, and the subsequent space charge calculation is based only on the remaining ions.

2. The degree of neutralization of space charge can be studied by using only a percentage of the full space charge force.

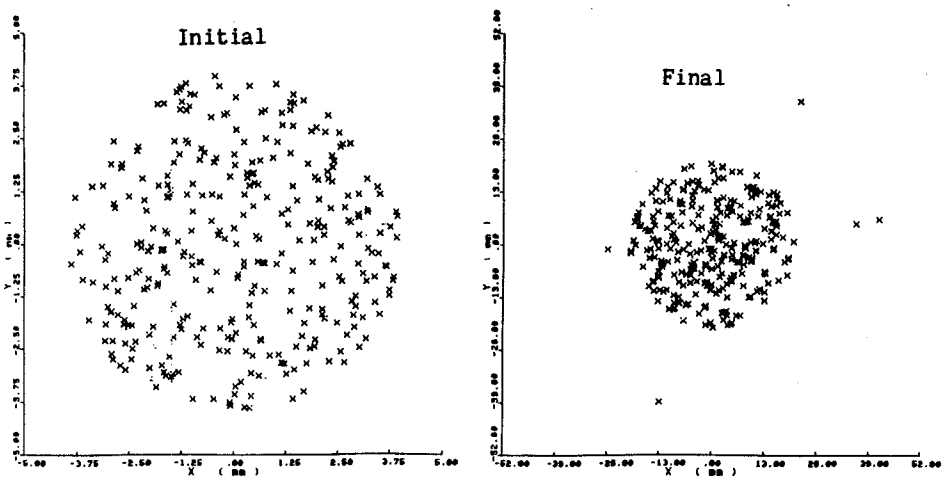


Figure 2.6. The initial and final ion position distributions.



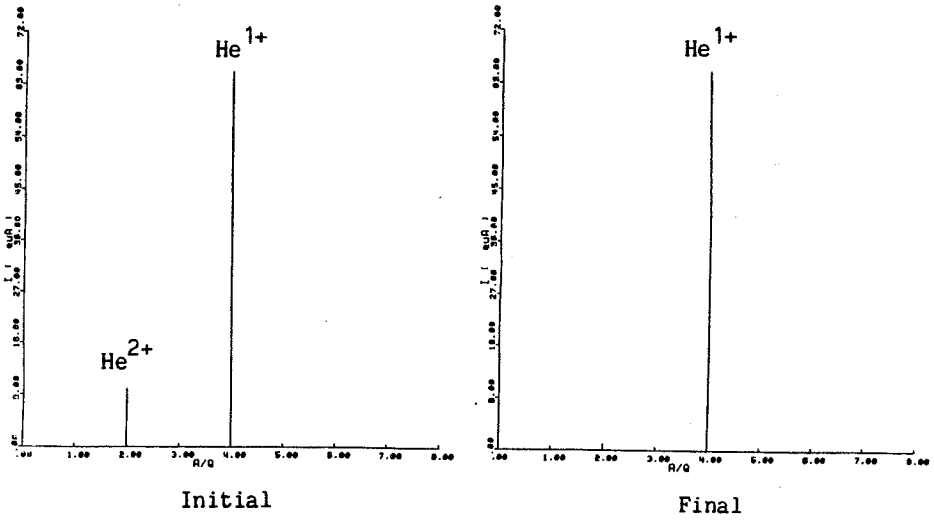


Figure 2.7. The initial and final charge state distributions (CSD).

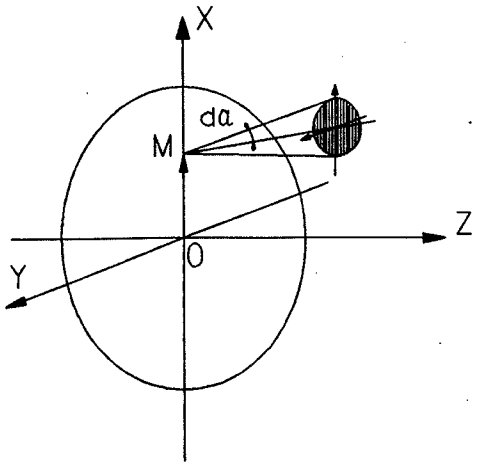


Figure 3.1. Schematic cross section of a beam.



simultaneously. However, we generally are interested in the emittance of an ion beam of single species within this ensemble. We will use the term "beam" to refer to a beam of a single ion species unless otherwise specified in the text.

The emittance of a beam with rotational symmetry in the phase plane is described by an ellipse, as shown in Figure 3.2, and this ellipse is described by the following equation, in generalized x-x' transverse coordinates

$$\left(\frac{Ax'-Bx}{a}\right)^2 + \left(\frac{Ax+Bx'}{b}\right)^2 = 1 \qquad (3.3)$$

where $A = \cos\theta$, $B = \sin\theta$ and a and b are the minor and major axes of the ellipse as shown in Figure 3.2. Let D(X) denote the distance between two points (1,2) on the ellipse with the same x coordinate

$$D(x) = x'(1) - x'(2) \qquad (3.4)$$

Solving Eq. (3.3) yields

$$x'(1) = \frac{1}{A^2b^2 + B^2a^2}\left[AB(b^2 - a^2)x + ab(A^2b^2 + B^2a^2 - x^2)^{1/2}\right] \qquad (3.5)$$

$$x'(2) = \frac{1}{A^2b^2 + B^2a^2}\left[AB(b^2 - a^2)x - ab(A^2b^2 + B^2a^2 - x^2)^{1/2}\right] \qquad (3.6)$$

thus D(x) is given by

$$D(x) = \frac{2ab}{A^2b^2 + B^2a^2}(A^2b^2 + B^2a^2 - x^2)^{1/2} \qquad (3.7)$$

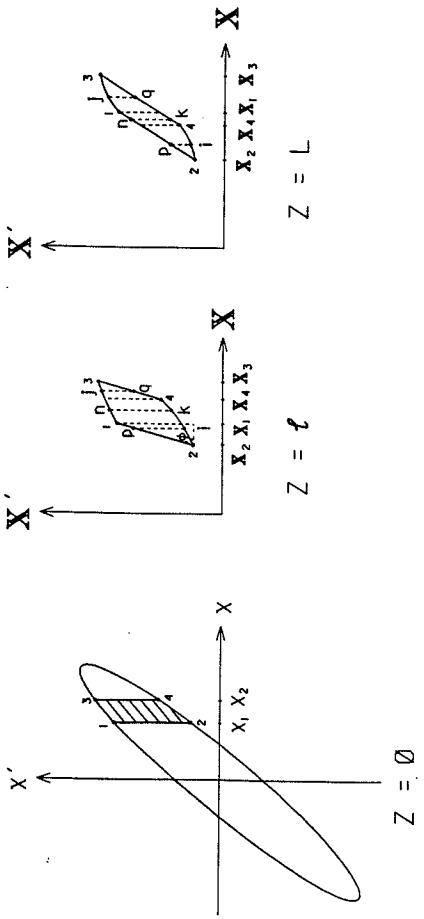


Figure 3.3. The particles which lie in the shaded area of the shown ellipse (z = 0) will evolve to either of the cases in B (z = l) or C (z = L) after a drift distance.



$$X_3 = x_2 + lx'(3) \qquad X'(3) = x'(3)$$

$$X_4 = x_2 + lx'(4) \qquad X'(4) = x'(4) \tag{3.9}$$

Graphically one can see that

$$\text{Tan}\phi = \frac{X'(1) - X'(2)}{X_1 - X_2} = \frac{X'(1) - X'(2)}{l[X'(1) - X'(2)]} = \frac{1}{l} \tag{3.10}$$

then the divergence of particle p on the line 1-2 would be

$$X'(p) = x'(2) + (X_i - X_2)\text{Tan}\phi_1 = x'(i) + \frac{x_i - x_1}{l} \tag{3.11}$$

Thus the vertical distance between point p and point i is given by

$$D(X)_{p-i} = X'(p) - X'(i) = \frac{x_i - x_1}{l} \qquad X_2 \leq X_i \leq X_1 \tag{3.12}$$

likewise, the distance between X'(j) and X'(q) is

$$D(X)_{j-q} = \frac{x_2 - x_1}{l} \qquad X_4 \leq X_j \leq X_3 \tag{3.13}$$

In the interval between $X_4$ and $X_1$, the vertical distance between points n and k is determined by

$$D(X)_{n-k} = \frac{x_k - x_n}{l} \qquad X_1 \leq X_k \leq X_4 \tag{3.14}$$

Although $x_1$ and $x_2$ are known, the other $x_i$ between region $[x_1, x_2]$ are not. In order to have a distribution of D(X) in the X-X' coordinates,

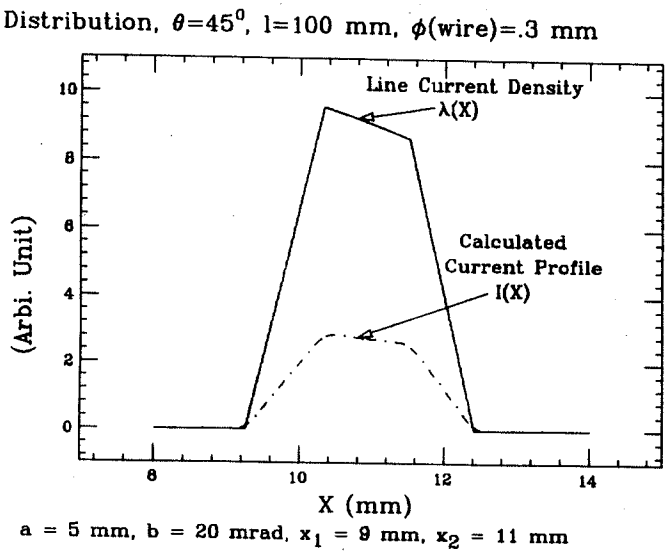


Figure 3.4. A comparison, for the case Figure 3.3B, with drift distance 100 mm, of the line current density and the calculated current profile as measured with a wire of 0.3 mm wide. The particles were initially in the area determine by $x_1$ = 9 mm and $x_2$ = 11 mm for an ellipse with a 45° orientation, a = 5 mm and b = 20 mrad, at z = 0.



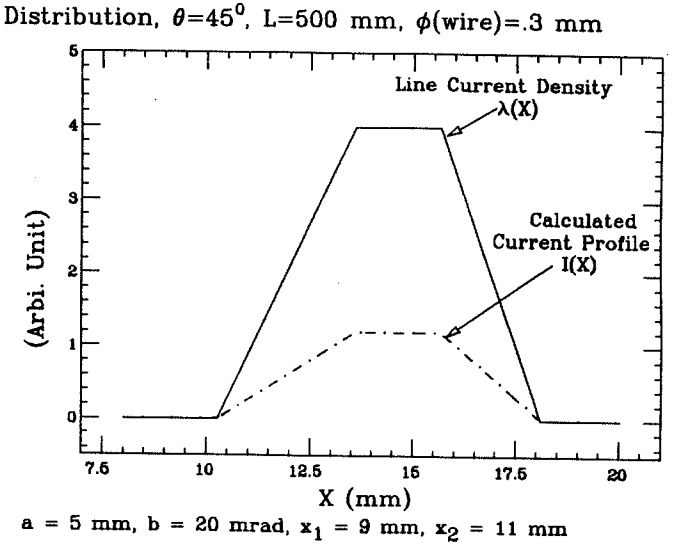


Figure 3.5. A comparison, for the case Figure 3.3C with a drift distance 500 mm, of the line current density and the calculated current profile as measured with a wire of 0.3 mm wide. Other conditions are the same with the case in Figure 3.4.

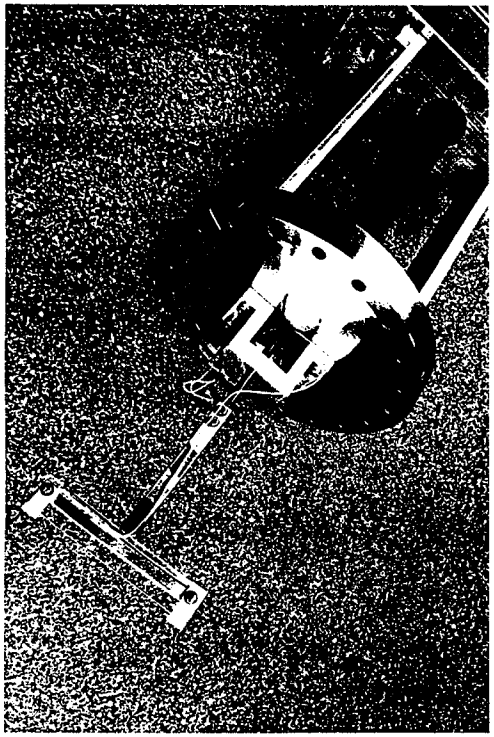

Figure 3.6. The assembly of the wire scanner.



The wire output signal and the wire position information are recorded by computer and can be analyzed on line to give the beam profile and the emittance in one transverse phase plane. In this analysis program, the beamlet edge determinations are based on the arguments outlined in Section 3.1. The divergences x'(i) versus the positions $x_i$ are determined, and the emittance is then estimated by an ellipse fitting routine. One can measure the beam profile and emittance in the other transverse phase plane by rotating the whole setup 90°. Figure 3.7 shows an $Ar^{10+}$ beam emittance measurement made with this slit-wire scanner.

### 3.3 Kapton Camera

As mentioned in Chapter 1, we have also made Kapton foil burns, with a beam defining slit plate (of slot size .010" x 2.8", 3~4" upstream of the foil), to measure the helium beam profiles and emittances. This method of course can also be used to measure other beam profiles and emittances after the analysis magnet where a beam of single ion species is selected. The advantage of using this technique is that the device required is simple and gives two dimensional information (both transverse directions) at the same time, while the wire scanner moves only in one direction. It also shows coherent effects such as relative beam motion and multiple beams, which is very useful for interpreting other beam profile measurements. The disadvantage of such method is that frequent venting of the beamline vacuum may be required to remove foils. In order to reduce the beamline vacuum venting, we have designed a Kapton camera which can do 10 to 12 foil burns.

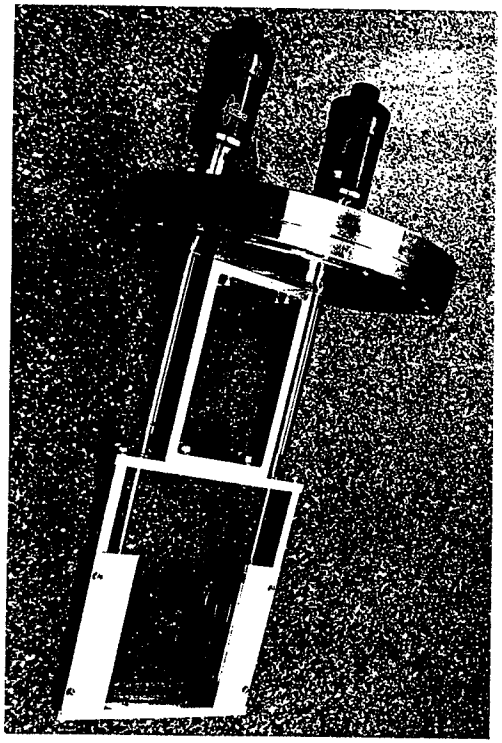

Figure 3.8. The assembly of the 'Kapton camera'.



# Chapter 4

## Extraction Geometry Study

### 4.1 Motivation

The ion beam extraction system is usually located near the peak field of the end mirror. The most common extraction system that has been used to form beams of ions from ECRIS is shown schematically in Figure 4.1A. It is a three electrode system with applied voltages $V_a$, $V_b$ and $V_c$ on the relevant electrodes respectively. Positive ions are expelled from the source and the beam transport line is at ground potential, which results in the requirements that $V_c = 0$ and $V_a > 0$. The intermediate electrode with voltage $V_b$ is used to obtain adequate ion focussing. The beam energy is determined by $V_a - V_c = V_a$, which is set by the application, while the voltage difference $V_a - V_b$ and the spacing D between these two electrodes determine the maximum current that can be extracted from the source for a given plasma. The variation of the voltage $V_b$ from negative to positive will enable the extraction system to be one of the 3 cases: 1. accel-decel ($V_b < 0$), as illustrated in Figure 4.1B, the region between $V_a$ and $V_b$ is accelerating and radially focussing while the region between $V_b$ and $V_c$ is with decelerating and defocussing, though the net effect of the extraction system is focussing if the focussing strength in the acceleration gap is stronger than the defocussing strength, 2. accel-only ($V_b = V_c = 0$, electrode b and c can be combined as one), as shown in Figure 4.1C, which produces only a focussing effect in the region between $V_a$ and $V_b$, 3. accel-accel ($V_a > V_b > 0$), as shown in Figure 4.1D,